Journal of Wind Engineering & Industrial Aerodynamics 206 (2020) 104365

Contents lists available at ScienceDirect

Journal of Wind Engineering & Industrial Aerodynamics

journal homepage: www.elsevier.com/locate/jweia

Aerodynamic forces on iced cylinder for dry ice accretion – A numerical study

Pavlo Sokolov *, Muhammad Shakeel Virk

Institute of Industrial Technology, University of Tromsø, The Arctic University of Norway, Norway

ARTICLE INFO

Keywords:
Atmospheric icing
Cylinder
CFD
Numerical
Angle of attack
Drag
Lift
Transient
Comparison

ABSTRACT

Within this paper the ISO 12494 assumption of standard of slowly rotating reference collector under ice accretion has been tested. This concept, introduced by (Makkonen, 1984), suggests that the power line cables, which are the basis of the "reference collector" in the ISO framework, are slowly rotating under ice load, due to limited torsional stiffness. For this purpose, several Computational Fluid Dynamics (CFD) simulations of the atmospheric ice accretion and transient airflow conditions over iced cylinder at different angles of attack were performed. In order to ascertain the similarity, several parameters were chosen, namely, drag, lift and moment coefficients, pressure and viscous force. The results suggest that the benchmark cases of rotating and uniced cylinder have "similar" aerodynamic loads when compared with the "averaged" results at different angles of attack (AoA), namely, the values of total pressure and viscous force. However, on individual and instantaneous basis the difference in the airflow regime between AoA cases and the benchmark cases can be noticeable. The results from the ice accretion simulation suggest that at long term the gravity force will be the dominating one, with rotating cylinder being a good approximation to the "averaged" angle of attack cases for the ice accretion.

1. Introduction

The study and modeling of the atmospheric icing of structures is of a prime importance in ice-prone regions, in particular in the High North. The primary importance of it lies in the estimation of ice loads on objects, in order to evaluate potential threats of damage on infrastructural objects due to the accreted ice. At present, the aggregated knowledge on atmospheric icing of structures, as well as modeling and measuring guidelines for ice loads are being governed by the ISO 12494 standard "*Atmospheric Icing on Structures*" (ISO, 2001). When it comes to modeling and classifying the ice loads under its' framework, one of the primary key points in the ISO 12494 is the notion of a "reference collector" – a slowly rotating 30 mm in diameter cylinder by 500 mm in length. The notion of using a rotating cylinder is of a particular interest, and, sometimes, its usage results in questions.

The choice of a rotating cylinder as a reference collector can be explained by several reasons. First, the usage of a rotating cylinder results in uniform shape of accreted ice, which is rather simple to model, as the cylinder's cross-section, remains circular throughout entire period of the ice accretion, and any possible effects, arising due to a potentially asymmetric shape in the icing of a non-rotating cylinder, are not applicable in the rotating case. This simplifies the analytical model procedure significantly. Second, the Finstad et al. icing parameterization (Finstad et al., 1988) which is the main part of theoretical modeling in ISO 12494, and has been independently verified by Makkonen and Stallabrass (1987) assumes the rotating cylinders. Lastly, the idea of using a rotating cylinder in the modeling of the ice accretion was originally proposed by Makkonen (1984) in connection to the power line icing. The primary assumption behind this is that the conductor cable is slowly rotating under induced loading, due to limited torsional stiffness of the conductor cable.

The phenomenon of rotation of the power line cables under icing loads has been widely observed in nature, with the ice shape being circular under long term conditions, both as referenced in Makkonen (1984). However, to the best of authors' knowledge, this exact treatment of this phenomenon received very limited experimental investigation, in particular, when it comes to the start of the rotation and the rate of rotation of the cable under ice loads. Only (Makkonen and Stallabrass, 1984) have performed some experimental investigation, on a model wires, approximately 1 and 4 cm in diameter, attached to the springs, to emulate the torsional stiffens of an actual wire. In the wind tunnel experiments they have measured the rotation rates of 65 and 224°/hr for 1

* Corresponding author.
E-mail address: pavlo.sokolov@uit.no (P. Sokolov).

https://doi.org/10.1016/j.jweia.2020.104365
Received 12 March 2019; Received in revised form 23 August 2020; Accepted 23 August 2020
Available online 28 September 2020

and 4 cm "wire" respectively. Again, as referenced in Makkonen (1984), the cause of rotation of power lines is attributed to the limited torsional stiffness of power line against the force, caused by the gravity of the accreted deposit.

This has certain potential implications for the ice modeling on power lines, in conjunction with the previously postulated assumption of uniform slow rotation. If the rotation rate is slow, or happens only in large "increments" after the significant icing load is accumulated first, the accreted ice shape is not going to be uniform, unless a large time interval is used in the modeling of icing, which can negatively affect the accuracy of it. Moreover, while the gravity has been so far assumed to be the dominating factor causing power line rotation, to the best of authors knowledge there have been no rigorous attempts to quantify the aerodynamic forces, generated by the iced conductor in cross flow, and their potential impact on power line cables rotation.

Therefore, this study attempts to addresses some of the potential effects of these. The main purpose of this work is to ascertain, using a series of CFD based numerical simulations, how the aerodynamic forces and the airflow behavior around iced cylinder change for a number of different angles of attack. It is believed that such analysis can assist and supplement in the estimation of the combined effects of wind and atmospheric icing, for example, in the methodology, attempted by Rossi et al. (2020). The comparison of obtained results is made against the rotating cylinder case, in order to check if the ISO 12494 approach of "reference collector" and rotating conductor assumption are a representative way of modeling the icing events on power lines under slow rotation assumption as postulated by Makkonen (1984). This is done by comparing drag, lift and moment coefficients in addition to Strouhal number and total pressure and viscous force of an iced cylinder as primary descriptors of "flow similarity".

2. Design of experiment

2.1. Operating conditions

As a baseline for comparison, the case no. 2 from Fu et al. (2006) has been selected. This particular choice was governed by several reasons, namely the need to select the case with known experimental ice shape, under "dry growth" conditions, and with the cylinder diameter, which is representative of a diameter of a power line conductor. In particular, having the information on the experimental ice shape allows for an ease of validation of the numerical results, while operating with the "dry growth" conditions reduces the amount of variables that can influence the ice growth. The operating conditions for this study are given in Table 1, while the comparison between the simulated ice shape at 0° AoA and the experimental shape from Fu et al. (2006) is shown in Fig. 1. Since the droplet distribution spectrum information was not provided in Fu et al. (2006), the simulations were performed using Langmuir D distribution, as it is a common distribution in the in-flight icing studies (Bidwell, 2012), (Papadakis et al., 2007), (Wright, 2008).

The main reason for choosing this particular combination of AoA's is to provide a decent coverage in the 0–90° quarter. Opting out of simulations with AoA more than 90° is based on the assumption that the results will be "symmetric" with respect to the 0–90° quarter. The numerical simulations of the ice accretion were performed at all AoAs

Table 1
Operating conditions.

Parameter	Value
Air speed (m/s)	5
Temperature (°C)	−15
MVD (μm)	35
Cylinder diameter (mm)	35
LWC (g/m^3)	1.2
Icing duration (min)	30
Angle of attack	0°, 30°, 60°, 90°

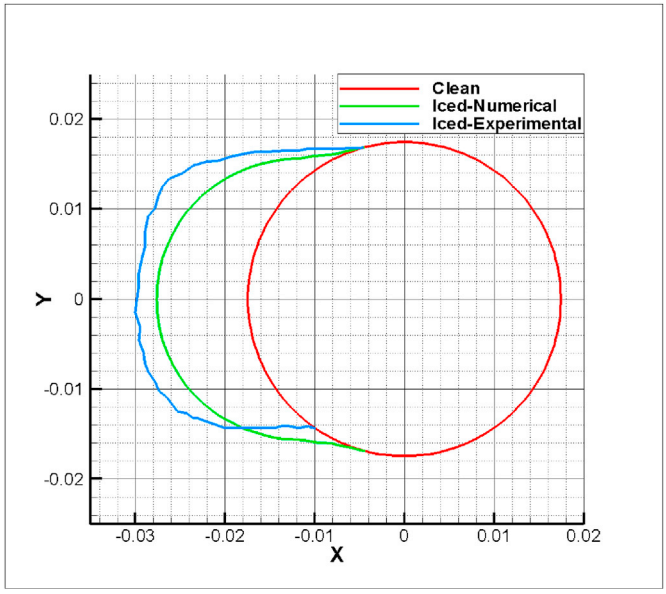

Fig. 1. Comparison of experimental and simulated ice shape.

specified in Table 1, while the transient airflow simulations were performed at 0° AoA for all cases. The reasoning for this is two-fold – first, is to investigate the effect of AoA on the ice accretion process and to keep the amount of variables in the airflow simulations to the minimum. In addition, the assumption of cable rotation happening only after the ice load has been accumulated on it has been made, which ties into the previously mentioned reasoning. For consistency purposes both the ice accretion and the transient airflow simulations were run with the same values for the characteristic length and area. These values are $D = 35$ mm, corresponding to the diameter of the uniced cylinder and $A = DL$, where A is the area, and L is the length of the object in z-direction, being equal to 1 m in all cases.

2.2. Numerical model

The multiphase CFD numerical simulations of ice accretion were carried out using ANSYS FENSAP-ICE, which uses Eulerian water droplet impingement solver. The existing analytical models of droplet behavior, for example, the ISO 12494/Finstad et al. solve droplet trajectories using Lagrangian particle tracking approach. The Eulerian method treats the particle phase as a continuum and develops its conservation equations on a control volume basis and in a similar form as that for the fluid phase. The Lagrangian method considers particles as a discrete phase and tracks the pathway of each individual particle. By studying the statistics of particle trajectories, the Lagrangian method is also able to calculate the particle concentration and other phase data. On the other hand, by studying particle velocity vectors and its magnitudes in Eulerian method, it is possible to reconstruct the pathways and trajectories of particles in a phase.

The general Eulerian two-phase model for viscous flow consists of the Navier-Stokes equations augmented by the droplets continuity and momentum equations (FENSAP-ICE User Manual)FENSAP-ICEFENSAP-I:

$$\frac{\partial \alpha}{\partial t} + \overrightarrow{\nabla} \cdot (\alpha \overrightarrow{V_d}) = 0 \tag{1}$$

$$\frac{\partial (\alpha \overrightarrow{V_d})}{\partial t} + \overrightarrow{\nabla}[\alpha \overrightarrow{V_d} \otimes \overrightarrow{V_d}] = \frac{C_D Re_d}{24K} \alpha (\overrightarrow{V_a} - \overrightarrow{V_d}) + \alpha \left(1 - \frac{\rho_a}{\rho_d}\right) \frac{1}{Fr^2} \tag{2}$$

where the variables α and $V_{d,a}$ are mean field values of, respectively, the water volume fraction and droplet velocity. The first term on the right-hand-side of the momentum equation represents the drag acting on

droplets of mean diameter d. It is proportional to the relative droplet velocity, its drag coefficient C_D and the droplets Reynolds number:

$$Re_d = \frac{\rho_a d V_{a,\infty} \overrightarrow{V_a} - \overrightarrow{V_d}}{\mu_a} \tag{3}$$

and the droplet inertia parameter:

$$K = \frac{\rho_d d^2 V_{a,\infty}}{18 L_\infty \mu_a} \tag{4}$$

Where L_∞ is the characteristic length of the object. In case of the cylinder the characteristic length is cylinder radius.

The second term represents buoyancy and gravity forces, and is proportional to the local Froude number:

$$Fr = \frac{V_{a,\infty}}{\sqrt{L_\infty g_\infty}} \tag{5}$$

These governing equations describe the same physical droplets phenomenon as Lagrangian particle tracking approach. Only the mathematical form in which these equations are derived changes, using Partial Differential Equations instead of Ordinary Differential Equations. The droplet drag coefficient is based on an empirical correlation for flow around spherical droplets, or:

$$CD = (24 / Red)\,(1 + 0.15Red0.687) \quad for \quad Red \leq 1300$$

$$CD = 0.4 \quad for\ Red > 1300$$

The local and overall collision efficiencies are calculated as follows:

$$\beta = \frac{\alpha \overrightarrow{V_d} \cdot \overrightarrow{n}}{w V_\infty} \tag{6}$$

where α is the local volume fraction (kg/m^3) and $\overrightarrow{n}$ is the surface normal vector. The overall collision efficiency is an integration of local collision efficiencies over surface area and is given as:

$$\beta_{tot} = \frac{\int \beta \, dA}{L_\infty^2} \tag{7}$$

Since the FENSAP-ICE is a 3D Reynolds-Averaged Navier-Stokes (RANS) solver a choice of turbulence closure for the RANS equations is needed. As it can be seen from operating conditions in Tables 1 and 2, the expected Reynolds number for the cylinder in numerical simulations is of an order of 1×10^4, thus the flow is fully turbulent. Moreover, detailed mesh sensitivity analysis was carried out to accurately determine the boundary layer characteristics (shear stress and heat fluxes), a $y+$ values of less than 1 is used near the cylinder wall surface. Number of mesh elements and $y+$ value was selected based upon the heat flux calculations, where a numerical check was imposed that the heat flux computed with the classical formulae dT/dn should be comparable with the heat flux computed with the Gresho's method.

Based on this information the turbulence model chosen for the FENSAP-ICE is the Menter's SST k-ω model. The detailed information on Menter's SST k-ω model is given in Menter (1994). The choice between the Spalart-Allmaras, low Re k-ω model and Menter's SST k-ω model in FENSAP–ICE was based on the robustness of the k-ω SST model in the near-wall region and the discussions in the (Elkhoury, 2016) about applicability of SA and k-ω SST models for the turbulent flow past bluff bodies. The surface roughness model used in CFD simulations is Shin et al. sand-grain roughness formulation (Shin and Bond, 1992). The accreted ice density model used in the numerical simulation was rime ice with Jones (rime) icing density model, given as (Jones, 1990):

$$\rho = 0.249 - 0.0840 ln\pi_C - 0.00624(ln\pi_\varphi)^2 + 0.135 ln\pi_K + 0.0185 ln\pi_K ln\pi_\varphi - 0.0339(ln\pi_K)^2 \tag{8}$$

where π_K is the droplet inertia coefficient, π_ϕ is the Langmuir parameter defined as:

$$\pi_\varphi = \frac{18\rho_a^2 L_\infty V_{a,\infty}}{\rho_d \mu_a} = \frac{Re_d^2}{K} \tag{9}$$

where Re_d is the droplet's Reynolds number. Finally, the term π_C is the ratio of the convective heat flux and the heat flux due to droplet freezing and is defined as:

$$\pi_C = \frac{k_a(-2T)/L_\infty}{w V_{a,\infty} L_f} \tag{10}$$

where L_∞ is the object characteristic dimension i.e., cylinder radius. The reason for choosing rime icing model and Jones (rime) icing density formulation in the numerical simulations was the fact that this particular combination provided the best match with experimental ice shape of Fu et al. (2006). After the icing simulation completion, the displaced grid was generated in FENSAP-ICE, using the Arbitrary Lagrangian-Eulerian (ALE) method.

However, since FENSAP-ICE is a 3D solver exclusively, and it was decided to perform transient airflow simulations using Ansys Fluent in 2D, for the purpose of computational efficiency, it was necessary to perform the "dimensional reduction" before the transient airflow simulations could be carried out. In order to do this, the.stl output files from the FENSAP-ICE were used and the mesh extension in z-direction was removed in order to use the displaced grid in the Fluent. For consistency, the Menter's k–ω SST model, along with Shin et al. surface roughness model has been used in ANSYS Fluent. The pressure based solver and the coupled scheme for the pressure-velocity coupling has been chosen in ANSYS FLuent. The spatial discretization employed is second order upwind and the transient formulation was set to the second order implicit. The time step chosen for the transient simulations is 0.7071 ms. The choice of time step is based on the assumption of Strouhal number being equal to 0.2 for cylinder for the value of cylinder Reynolds number range, as calculated from the operating conditions in Table 1. Thus by reverse calculation, the frequency of flow has been found and from there the time step has been obtained. The amount of iterations per time step has been set to 50, with 7500 total time steps, as this particular combination has been found to provide good convergence along with parameters of interest reaching the "steady-state". Thus, the total transient simulation time was approximately equal to 5.3 s.

The forces and moments in the ANSYS Fluent simulations are obtained as (Fluent User Manual)Fluent:

$$F_a = \overrightarrow{a} \cdot \overrightarrow{F_p} + \overrightarrow{a} \cdot \overrightarrow{F_\nu} \tag{11}$$

and

$$\overrightarrow{M_A} = \overrightarrow{r_{AB}} \times \overrightarrow{F_p} + \overrightarrow{r_{AB}} \times \overrightarrow{F_\nu} \tag{12}$$

where a is the specified force vector, F_p is the pressure force vector F_ν is the viscous force vector and r_{AB} is the moment vector. The values of C_D,

Table 2
Values of ice accretion parameters of interest.

AoA	Iced Area (mm^2)	Max. Ice Thickness (mm)	Ice mass (g/m)	Overall Droplet Collision Efficiency (α_1)	ρ (kg/m^3)	Mean Bead Height (mm)
0°	302.97	10.1	110.5	0.292	364.7	1.31
30°	257.77	8.5	109.3	0.289	424.0	1.24
60°	265.07	8.6	112.4	0.297	424.0	1.22
90°	157.67	6.3	72.35	0.191	458.9	1.35
Rotating	246.47	2.1	110.5	0.292	448.3	3.53

C_L and C_M, are obtained from the values of drag force F_D, lift force F_L, and moment M, by dividing these respective values by the term $\frac{1}{2}\rho v^2 A$, where A is the reference area and it is equal to 0.035 m^2. This area represents the projected area, as viewed normal to the flow and ρ and v are the reference values for air density and velocity, respectively. Finally, the operating conditions in the ANSYS Fluent simulations are matching those given in Table 1.

3. Results and discussion

3.1. Ice accretion

The primary purpose of this subsection is to establish if the rotating cylinder is a good approximation to a non-rotating one at different angles of attack, and if there are any significant differences in ice accretion process between them. The main parameters of interest in the ice accretion simulations are the ice shapes, iced areas, maximum ice thicknesses, overall collision efficiencies (α_1), mean values of iced surface bead height and the accreted ice densities. Fig. 2 shows the comparison of the ice shapes simulated in FENSAP-ICE at different AoAs (0–90°) for the incoming multiphase flow, while Table 2 shows the values of parameters of interest, mentioned previously.

In Table 2, the iced area is calculated by taking the geometry profile of the iced cylinder at any given AoA or a rotating cylinder, calculating its total area, and then importing the geometry of an uniced cylinder and subtracting its total area. The resultant value will be the area covered by ice accretion only and this area is the "iced area".

From Fig. 2, it can be seen that the only apparent difference is the maximum ice thickness, with ice shape at 0° AoA being the "thickest" and 90° being the "thinnest" with the results at 30° and 60° AoA having the maximum ice thickness values in-between and closely matching each other. From Table 2 it can be also seen that the iced areas also follow the exact same pattern, and the iced area for rotating cylinder is comparable to that of 30° and 60° AoA simulations. For the ice masses, all cases, with the exception of 90° AoA show good agreement among each other. This follows from the results of the overall collision efficiencies values, which also match well, with the maximum difference in values of E being within 0.01, again, with exception of 90° AoA.

The abnormal results in the ice accretion simulations of the cylinder at 90° AoA can be explained by the deficiency in the setup. The numerical deficiency for this particular case is that the mesh used for the simulations is an O grid and the ice accretions simulations have been performed by rotating the inflow angle. For the 90° AoA case the inlet and outlet boundary conditions "interface" coincides with the direction of the incoming flow. For the transient airflow simulations this is not the case as the incoming flow angle is 0° for all cases. This is considered an acceptable compromise, since the FENSAP-ICE is an Eulerian solver and changing the mesh just for this one case can cause additional differences to arise, as the Eulerian methods are mesh-dependent. Finally, the maximum surface roughness from beading is the same is all cases, and its equal to 3.53 mm. This is a rather large value, considering that Shin et al. surface roughness formulation gives a surface roughness value of 33 μm.

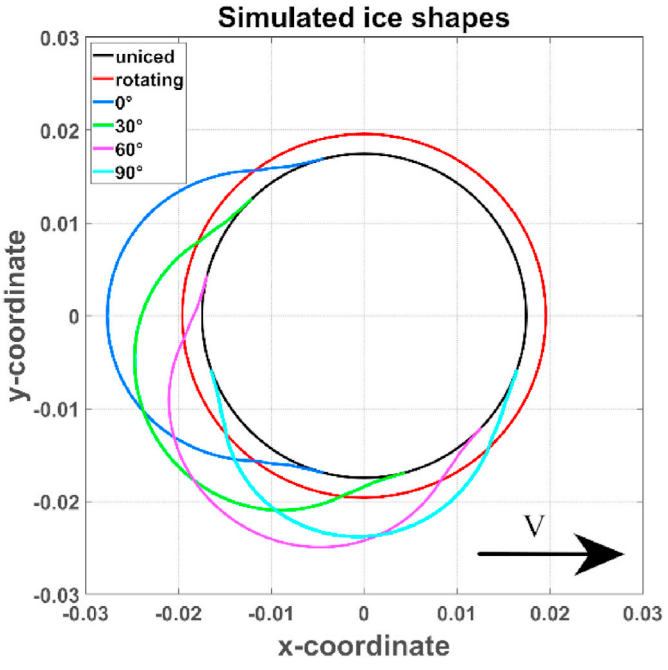

Fig. 2. Comparison of simulated ice shapes at different AoA.

Summarizing, when it comes to the ice accretion itself, the results of the simulations at different angles of attack and the rotating cylinder show good agreement, for the most parameters of interest. Since the dry growth regime in this study was maintained and verified from the mass balance in FENSAP-ICE, i.e., for all cases in this study, the masses of water film, water vapour etc. are all equal to 0, this means that the sticking and freezing efficiencies $\alpha_2 = \alpha_3 = 1$. Thus, from the ISO 12494 "*Atmospheric Icing on Structures*" modeling viewpoint:

$$\frac{dM}{dt} = \alpha_1 \alpha_2 \alpha_3 v w D L t \tag{13}$$

and since the operating conditions from Table 1 are the same, with the exception of the AoA, it follows that the ice accretions in this study are very similar. Therefore, for the accretion process itself, the rotating cylinder is a good approximation to the non-rotating cylinder at different angles of attack. However, this comparison is incomplete without investigating the flow behavior and aerodynamic forces across all cases in this study.

3.2. Airflow behavior

For the comparison of the airflow behavior of the different cylinder configurations, the plots of mean pressure distributions and velocity magnitudes and streamlines were obtained from transient airflow simulations, and they are given in Fig. 3 – 5, respectively.

The flow around cylinder at 0° AoA in Fig. 3 shows much more narrow wake, with the region of maximum negative pressure and the stagnation point pressure field are also narrower. This suggests that the flow separation occurs more gradually, and the flow "reconnects" past the cylinder in a similar, gradual fashion, as evidenced by low pressure zone in the wake of cylinder being rather protracted in x-direction. For the 30° AoA case the majority of "top side" is a pressure zone, while the "bottom side" is a suction zone, thus indicating that the cylinder experiences a downward acting lift. This coupled with the fact that the flow separation appears to be "gradual" similar to 0° AoA case and its unlike the 60° and 90° AoA cases, for which the pressure gradients are rather "sharp", thus indicating that 0° and 30° AoA cases should have lower values of C_D compared to 60° and 90° AoA cases.

On the other hand, the cylinder at 60° and 90° AoA experiences more significant pressure gradients and rapid flow separation, thus indicating that its subjected to the higher values of aerodynamic loads in these cases. Moreover, for the 60° and 90° AoA cases the stagnation pressure zone extends almost to the edges of the cylinder. This coupled with the significant pressure gradients in these cases suggests that maximum amplitude of aerodynamic loads, drag in particular, should be significantly higher for those cases than for the 0° and 30° AoA cases. Similar to the 30° AoA case, the cylinder at 60° AoA also shows the "top-side" of the cylinder being the pressure side, thus, again giving the indication of downwards acting lift. For the 90° case, however, the pressure distribution at the cylinder "edges" remains symmetric, similar to the 0° AoA case, thus indicating that for this case the C_L value should be very close to zero.

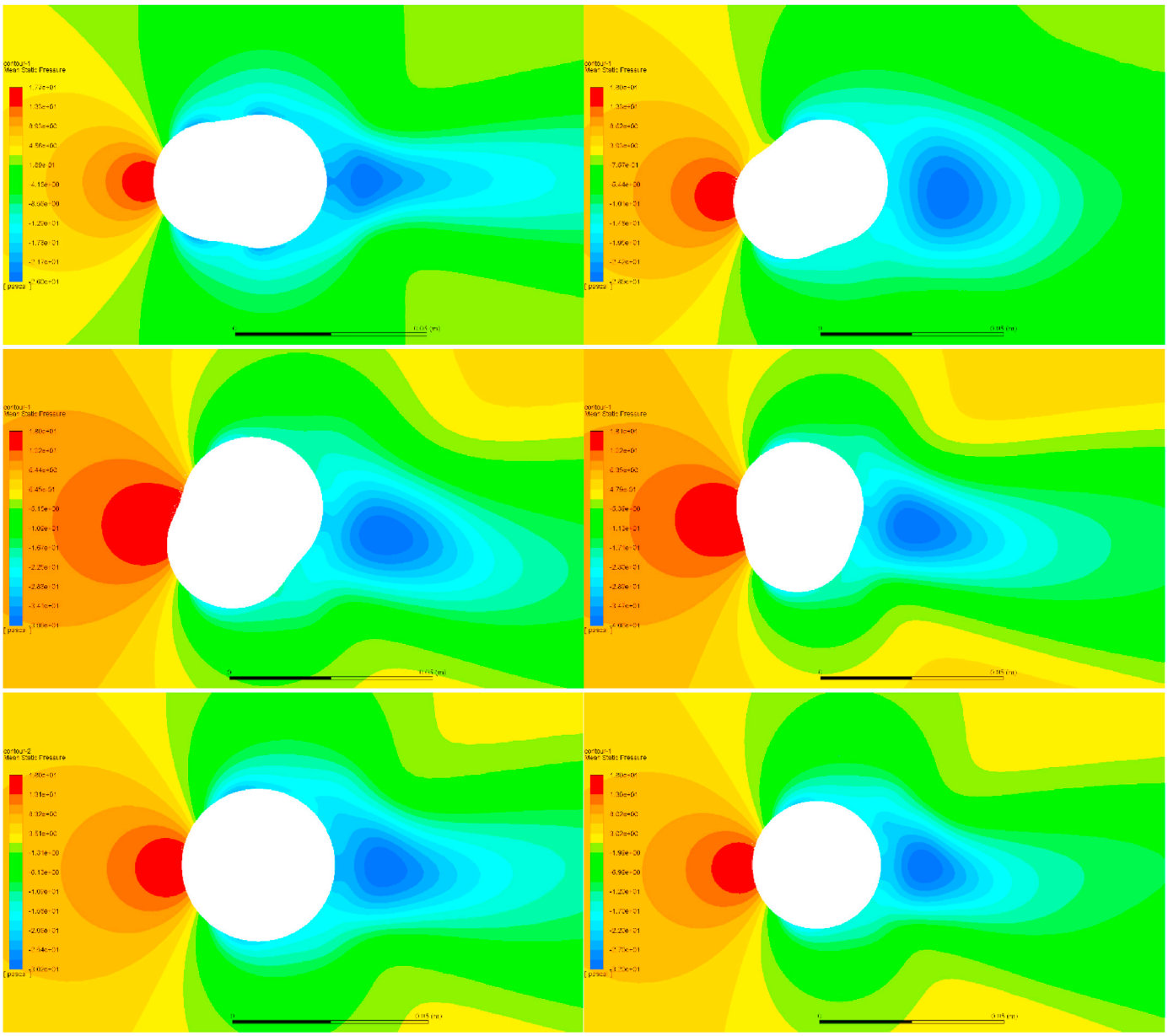

Fig. 3. Pressure distributions in numerical simulations. From top to bottom, left to right: 0°, 30°, 60°, 90° AoA, rotating and uniced cylinder. The values shown are the mean values across all time steps.

Comparatively, the benchmark cases of the rotating and the uniced cylinder, are in the "middle" between 0°, 30° and 60°, 90° AoA cases, as it is seen from Figs. 3 and 4, when it comes to flow field parameters, in particular the pressure distributions, as the pressure gradients and the extent of the stagnation pressure zones being "in-between" the 0°, 30° and 60°, 90° AoA cases. This by extension, implies that the aerodynamic loads, and in particular the drag values, should be higher than for 0° and 30° AoAs but lower than in 60° and 90° cases. Moreover, the same also true when comparing maximum negative pressures. The maximum negative pressures are −26 and −29 Pa for 0° and 30° AoA cases, respectively, while for 60° and 90° AoA cases, the maximum negative pressure is approximately −40 Pa for both cases. For the benchmark cases, these values are approximately −30 and −32 Pa for rotating and uniced cylinder, respectively. The maximum positive pressure is approximately 18 Pa for all cases. Thus, the results for the airflow behavior from Figs. 3 and 4 do suggest that there are differences in the instantaneous flow conditions in the transient CFD simulation present across all cases. This is further exacerbated by the instantaneous velocity streamlines plots, shown in Fig. 5. The characteristics of velocity streamlines change significantly between the reference cases of the rotating and uniced cylinders vs. the non-rotating iced cylinders. For the ice shape at 0° AoA the vorticity shedding occurs immediately past the cylinder, and for the cases with the ice shapes at non-zero AoA additional vortices are present behind the cylinder, when compared to the ice shape at 0° AoA. Again, in those cases the vorticity shedding starts immediately past the cylinder as opposed to the rotating and uniced cylinders, for which the shedding starts a bit further downstream. The turbulent shedding modes for the uniced cylinder are in good agreement with the turbulent shedding at $Re = 8 \times 10^3$ captured by smoke-visualizations in (Norberg, 2002), albeit the turbulent shedding in their case starts slightly further downstream than for the reference cylinder in this study.

Although the instantaneous flow behavior characteristics past different cylinders in this study does vary to a significant degree, the question, however, is how much these instantaneous differences can affect the aerodynamic loads, on the time frame of the typical icing event, with timeframes from minutes to hours.

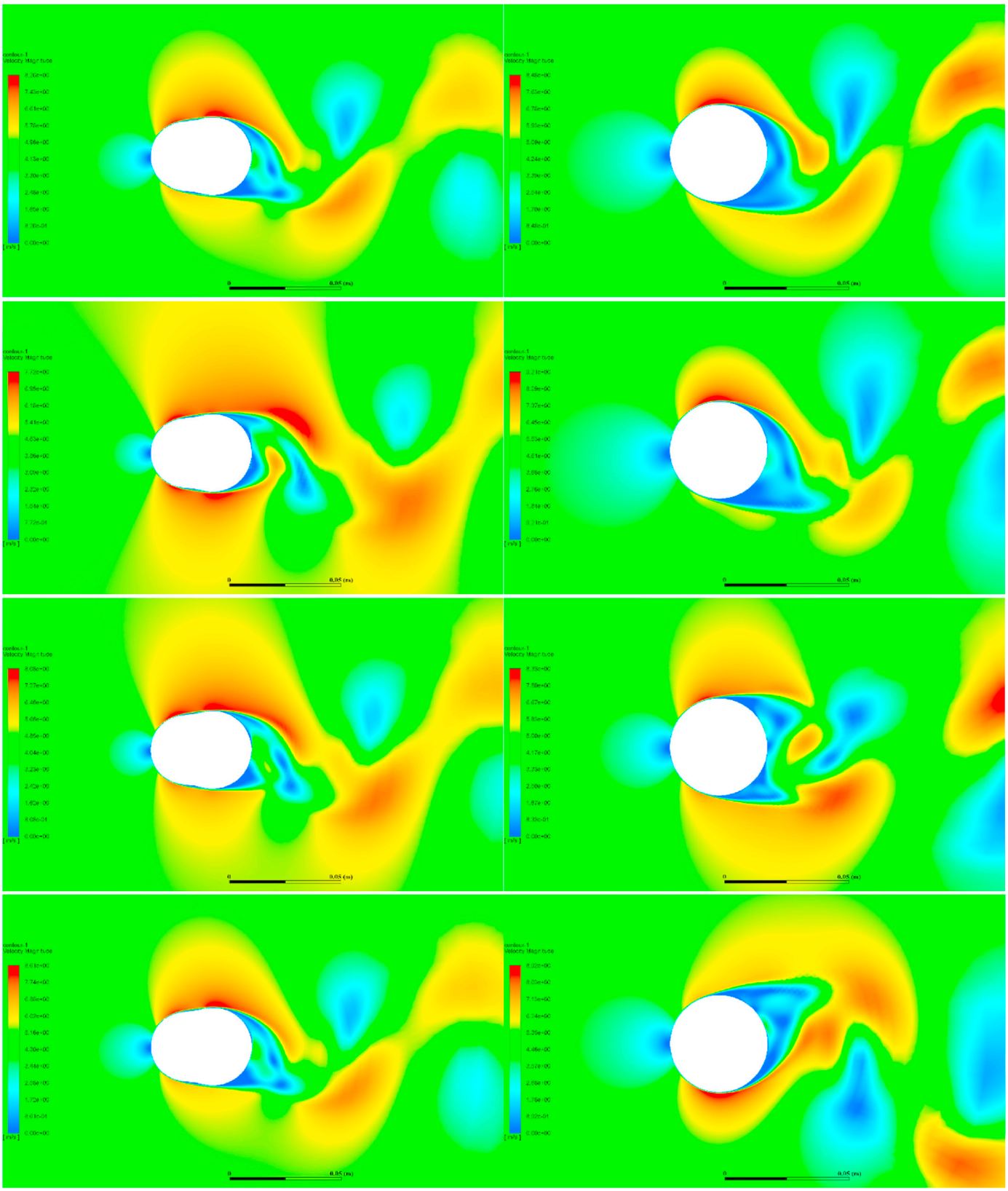

Fig. 4. Velocity magnitudes in numerical simulations for 0° AoA (left) and rotating (right) cylinder. From top to bottom the time step values are t = 1, 2, 3 and 5 s.

3.3. Aerodynamic loads

The transient airflow simulation results are presented in terms of combined plots of parameters of interest, namely the drag, lift and moment coefficients, combined pressure and viscous force (denoted as force) as well as the Strouhal number for all cases in this study. These plots are given in Fig. 6 and show the transient curves for the last 1.3s of the flow, which corresponds to approximately last 2000 time steps. To

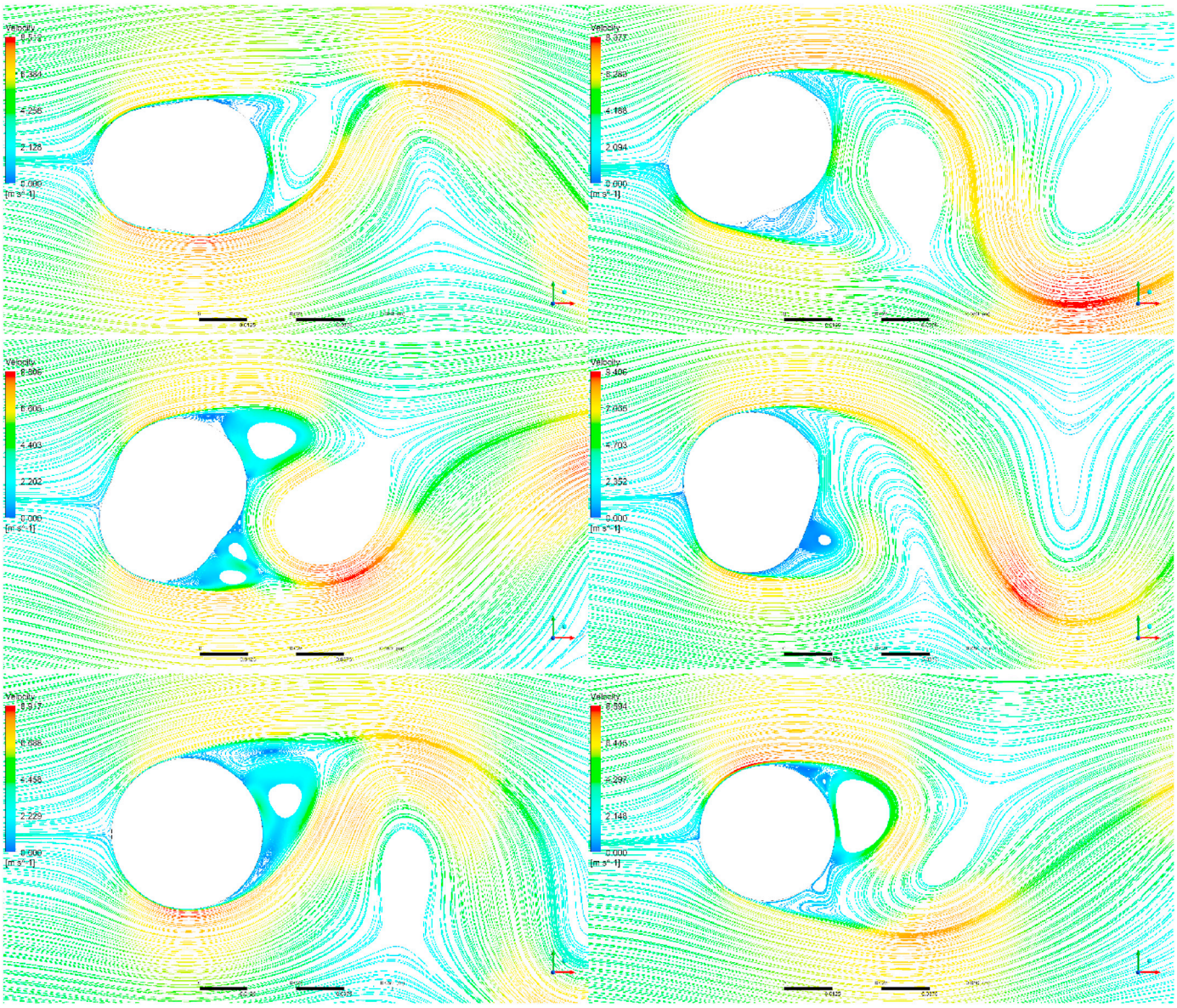

Fig. 5. Velocity streamlines in numerical simulations. From top to bottom, left to right: 0°, 30°, 60°, 90° AoA, rotating and uniced cylinder. The streamlines shown are for the last time step (t = 5.3 s).

avoid cluttering multiple different curves on a single plot, any given parameter of interest is presented by two subplots – first showing the values for the AoA cases, and second showing the values for the benchmark cases. In order to keep the comparison visually simple, the black curve, corresponding to 0° AoA case is presented in all subplots and the axis limits are kept consistent between the respective subplots.

Table 3 shows the mean values of C_D, C_L, C_M and total pressure and viscous force F, while the Strouhal number given in it corresponds to the value associated with the maximum magnitude. The mean values reported in Table 3 were taken from the last 2000 time steps of the airflow simulations, in order to avoid possible skewing of the resulting from taking into account the values at the beginning of the simulations, where results may not yet be converged.

The results from benchmark cases for the drag coefficient and Strouhal number compare favorably with the results of Relf and Simmons, as reported by Tanida et al. (1973) and Gerrard (1961), with C_D values in this work being slightly higher than these experimental values, possibly due to higher turbulence intensity in the numerical simulations in this work. Moreover, the C_D values of uniced and 90° AoA match closely those in the numerical simulations of Keyhan (2012) for the 5 m/s wind speed cases, and the C_D values with respect to angle behave in a similar trend, as in Rossi et al. (2020), even if their C_D values are different, due to different Reynolds number and the ice shapes. Moreover, the behavior of C_D and C_L curves and values, follows closely the ones in the (Selvam, 1997) for the uniced cylinder at $Re = 10^4$ who used Large Eddy Simulation (LES) in their study, contrary to the Unsteady Reynolds Averaged Navier-Stokes (URANS) in this work.

The comparison of the results from Table 3 with the experimental data of Demartino et al. (2013) shows that the obtained results follow similar trend to the case CC V2 in their work, in particular when it comes to the change in values of C_D, C_L and C_M. However, when it comes to magnitudes, especially for C_D their obtained values are somewhat lower than in this work, which can be explained by significantly higher values of *Re* in their experimental cases, arising from vastly different operating conditions, and thus it was deemed unnecessary to perform the comparison of ice accretion between this work and the experimental data of Demartino et al. (2013). Moreover, when it comes to their results it should be noted that aerodynamic forces and trends in magnitudes in the

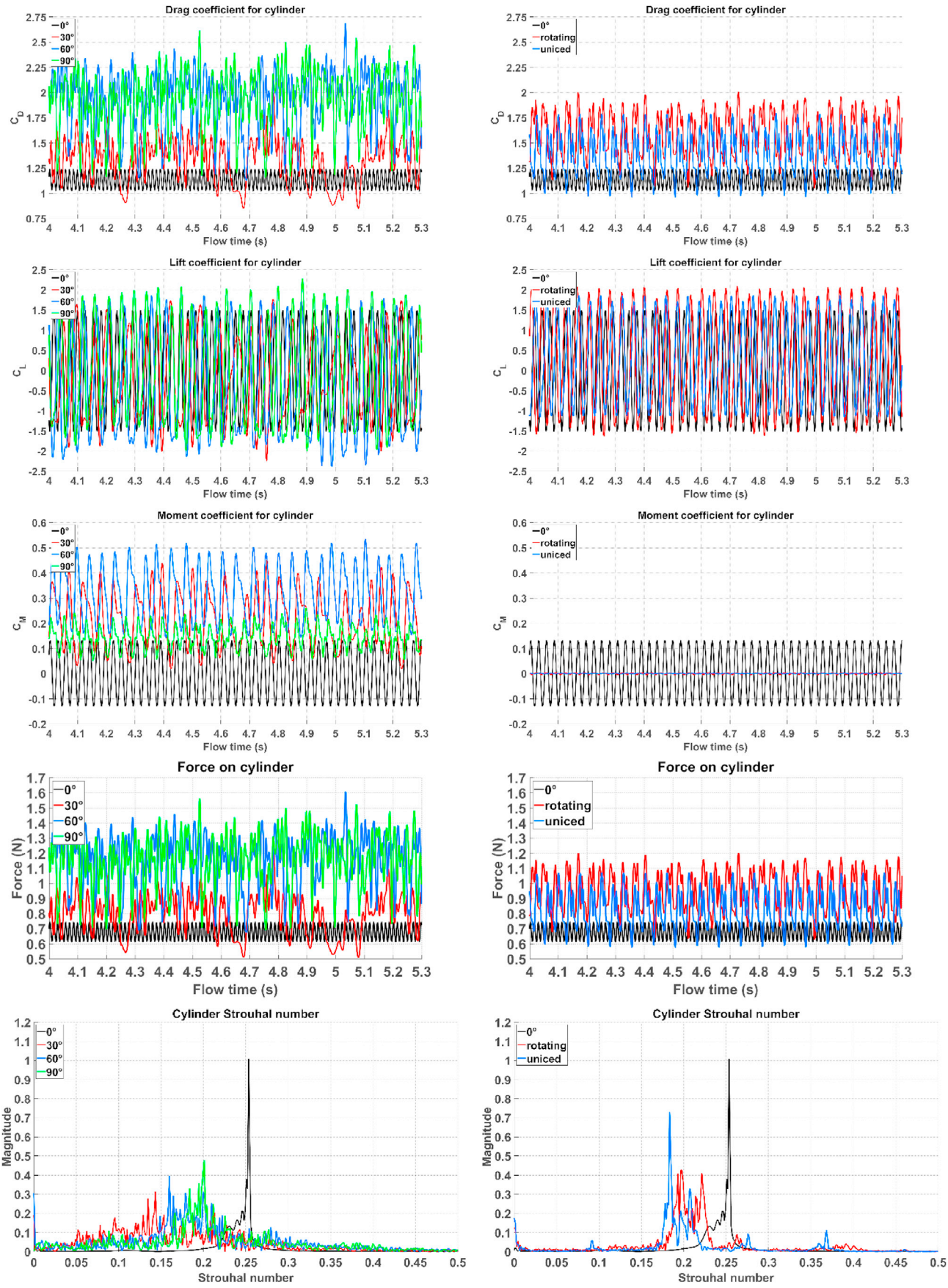

Fig. 6. Drag, lift, moment coefficients, force and Strouhal number values. The AoA values are given in legends.

Table 3
Values of parameters of interest in the numerical simulations.

Variable	0°	30°	60°	90°	Rotating	Uniced
C_D	1.13	1.34	1.93	1.93	1.58	1.38
C_L	−0.01	−0.21	−0.37	−0.03	0.26	0.27
C_M	0.00	0.21	0.32	0.15	0.00	0.00
F	0.68	0.79	1.16	1.15	0.95	0.83
Strouhal	0.25	0.14	0.16	0.20	0.20	0.18

experimental cases change significantly from one experimental case to another, even though the operating conditions do not change significantly. This fact, coupled with the results of numerical simulations in Keyhan (2012) show that the ice shape does have prominent effect on the aerodynamic loads.

Returning to the results in this work, the first interesting result, as inferred from Fig. 6 and Table 3 is that the iced cylinders at 0° and 30° AoA has smaller values of the drag and total pressure and viscous force, when compared to the rotating iced and uniced cylinder benchmarks. Several possible explanations of these phenomena can be made. First, the cylinder shape, especially for the 0° AoA case is rather streamlined, which may result in flow separation to be more gradual when compared to rotating and/or uniced cylinder. Second, is the airflow behavior around the cylinder, as discussed in the previous section. Moreover, it also can be observed from Figs. 1 and 2, that the leading edge of the iced cylinder is smaller than the diameter of an uniced cylinder. Finally, since all numerical simulations have used Shin et al. surface roughness model, the actual effect of iced surface roughness for the iced cases can be underestimated when compared to the uniced cylinder.

The cylinder at 30° angle of attack also experiences lower average values of the drag coefficient and force when compared to the uniced and rotating cylinder, however, the amplitude of fluctuation of C_D and F is higher than in benchmark cases. Again, same arguments can be made in this case as with 0° AoA case as to why the mean values of C_D and F are lower however, the significant amplitude of C_D and F fluctuations does suggest that this configuration can experience more significant aerodynamic loading, at maximum, than the benchmark cases. As for the 60° and 90° AoA cases, they exhibit an "expected" behavior, i.e., higher values of all the parameters of interest and higher amplitude of fluctuations. This suggests that the cylinder in these cases experiences higher aerodynamic loads than the reference cases of rotating and uniced cylinders. Furthermore, the moment coefficient is higher in the cases of 30° and 60° AoA, as compared to 90° AoA. A possible explanation here is that the 90° AoA is a mostly "symmetric" situation, with this sort of symmetry naturally reducing the C_M value, also indicated by the C_L value being zero for this case, as expected from the "symmetric" situation.

In addition, the positive moment convention in the numerical simulations is the counter-clockwise, thus the positive value of C_M for the 30°, 60° and 90° AoA cases indicate their tendency to pitch in the leading edge "down" direction, towards the increase in the value of AoA. On the other hand, the C_M value for the 0° AoA is expectedly zero, however, the amplitude of fluctuation of it is not, thus indicating that this configuration is prone to oscillation around $y = 0$ line. Finally, it is interesting to note the similarity of mean values of C_D and F for the 60° and 90° AoA cases. This can be explained, by the deficiencies of the numerical setup for the 90° case in the ice accretion simulations, as was discussed previously. As a consequence of it, the 90° shape in the simulations is not as "thick" as it should have been, thus resulting in 90° AoA case being less of an "obstacle" to the flow, in the geometric sense of it.

However, several peculiarities have been observed in the results in Fig. 6 and Table 3. First, the similarity in the amplitude of C_L values in the results for all tested configurations. While the maximum C_L oscillations do increase with change of configuration, for example, changing from 0° to 90° AoA, the magnitude of the fluctuations is not nearly as close as amplitude fluctuations in C_D values. This indicates that while configurations at extreme AoAs are more aerodynamically loaded, in absolute terms, they are just marginally more loaded in C_L terms. Second, is the non-zero C_L values for the uniced and the rotating cylinders, with the C_L being equal to 0.27 and 0.26, respectively. This may indicate possible asymmetry of the flow separation from the cylinder edges. When comparing these C_L values with an available results for the circular cylinder at the Reynolds number $Re = 10^4$ the results in this study for the circular cylinders are on the low range of the C_L values as measured in experiments by Gopalkrishnan (1992) with mean value of stationary circular cylinder C_L being 0.38.

Finally, the Strouhal number values, obtained from the C_L oscillations show a wide range of values, from 0.14 for the 30° AoA case to the 0.25 for the 0° AoA case. From reverse calculation, the frequency values of 36, 18, 19, 24, 25 and 26 Hz for the lift force oscillations were obtained, for the 0°–90° AoA, rotating and uniced cylinder, respectively, and twice the indicated frequencies for the drag force oscillations. The respective values, obtained from the Fast Fourier Transform (FFT) in Fluent are within ±1 Hz. Therefore, the cylinder at 0° AoA tends to have higher frequency of vortex shedding at smaller amplitudes, while 30° and 60° AoA cylinder have considerably higher amplitudes at smaller frequency. The 90° AoA and the benchmark cases fall in-between, and thus, the rotating cylinder "equivalence" assumption compares favorably.

Summarizing, since the cases with the 0° and 30° AoA are less aerodynamically loaded, while the 60° and 90° AoA cases are more aerodynamically loaded than the benchmark cases of the rotating and the uniced cylinder. It suggests that the "averaged" values across all 0–90° AoA cases should be comparable to the benchmark, and thus the "rotating" assumption should be mostly equivalent. To illustrate this, Fig. 6 shows the averaged values of total pressure and viscous force vs. benchmark cases. The total pressure and viscous force has been chosen as a parameter to compare, as it is independent of reference length and area in the numerical simulation, thus being the most "direct" way of comparing the results.

The results from Fig. 7 tend to support this previous assumption, as the combined F curve lies mostly on the rotating cylinder F curve in the steady state range, with mean value of F for the "averaged" curve being 0.95 which matches the value for rotating case from Table 3 within the rounding error. Thus, from the viewpoint of total aerodynamic force, acting on the cylinder, the rotating cylinder is equivalent to the "averaged" case of 0°–90° AoA.

Speaking about gravity force and their comparison with the aerodynamic forces, the following relation can be used to estimate the drag force per unit length for circular cylinder (Tritton, 1988):

$$C_D \equiv \frac{f_D}{\frac{1}{2}\rho v^2 D} \tag{14}$$

where f_D is the drag force per unit length. Using the value of C_D for the 0° AoA case from Table 3, as the drag force is the most significant aerodynamic force, the drag force per unit length obtained for that

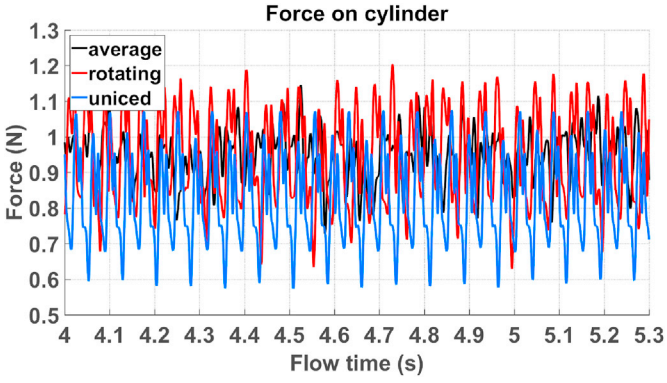

Fig. 7. Averaged drag coefficient vs. benchmark cases.

particular case is 0.68 N/m, using the previous relation. Using the value of accreted ice mass per unit length from Table 3, and using the operating conditions from Table 1 in calculations, the gravity force per unit length for the 0° AoA case is 1.08 N/m. Thus, already after 30 min of ice accretion, the gravity force is larger than the drag force, and it should continue to rise as the ice accretion continues, while the drag force won't be increasing as much, unless a significant change in configuration occurs. While this analysis is rather simplistic in nature it does show that while the drag force is proportional to the product of characteristic length and wind speed as Dv^2, given sufficiently large time frame of continued ice accretion, the gravity force, caused by this ice accretion will eventually dominate the aerodynamic forces, acting on cylinder. However, the exact time dependent model, mechanisms and their impact on actual rotation and twisting of the power lines are deemed to be too extensive to be properly developed in this work, although, the provided quantitative baseline, done in this work, does provide some insights into this matter.

4. Conclusion

Within the scope of this work numerous CFD simulations of the atmospheric ice accretion and the transient airflow behavior over iced cylinder with different angles of attack were performed. The objective was to investigate how commonly postulated assumption of slow, continuous rotation on a reference collector and/or power line (ISO, 2001), (Makkonen, 1984) compares with non-rotating iced cylinder at different angles of attack, which is deemed to be representative of very slow and/or spontaneous rotation. For the basis of comparison several flow parameters have been chosen in order to ascertain similarity, namely, ice shapes, maximum ice thicknesses and iced areas, accreted ice mass, ice densities, overall collision efficiencies, drag, lift and moment coefficients, pressure and viscous force, velocity magnitudes and pressure distributions.

The obtained results compare favorably for the hypothesis of rotating cylinder being "equivalent" to the series of non-rotating cylinder at different AoAs. In particular, the results tend to agree very well for the comparison of ice accretion parameters, where all cases, with the exception of 90° AoA, compare well to the rotating cylinder benchmark. The discrepancy in the 90° AoA case can be explained by the deficiencies in the numerical setup.

The comparison of the aerodynamic forces suggests that the benchmark cases of rotating and uniced cylinders, do have "similar" aerodynamic loads when compared to the "averaged" AoA simulations results, namely, when it comes to the values of total pressure and viscous force, which for the "averaged" case matches the rotating one within the rounding error. However, on individual basis the difference in the airflow regime between AoA cases and the benchmark cases can be significant, particularly, if checking the instantaneous values for the velocity magnitudes and pressure distributions in the transient airflow separation. In particular, the results from small AoA simulations (0° and 30°) show that the cylinder is less aerodynamically loaded than the benchmark cases. On the other hand, the results from simulations at large AoA (60°and 90°) produced "expected" results, as the cylinder in these configurations is significantly more aerodynamically loaded than the reference cases. However, as it was discussed previously, given sufficient enough time frame for continued ice accretion, the gravity force, exerted by the accreted ice deposit, will, eventually, be the dominating force, however, the exact situation will depend on the operating conditions and the shape of the developing ice deposit.

The comparison of the results from this work with the results of numerical simulations of Keyhan (2012) and experimental data of Demartino et al. (2013) shows good agreement, where applicable, however, one apparent trend in both (Keyhan, 2012) and (Demartino et al., 2013) is that the resultant aerodynamic loads are not only a function of Reynolds number but the accreted ice shape as well.

CRediT authorship contribution statement

Pavlo Sokolov: Writing - original draft, Investigation, Formal analysis, Visualization, Software, Data curation. **Muhammad Shakeel Virk:** Writing - review & editing, Conceptualization, Methodology, Resources, Supervision, Project administration, Funding acquisition.

Declaration of competing interest

The authors declare that they have no known competing financial interests or personal relationships that could have appeared to influence the work reported in this paper.

Acknowledgment

The work reported in this paper is funded by the Research Council of Norway, FRonTLINES- Project no. 245370 & IceBOX-Project no 282403.

References

Bidwell, C.S., 2012. Particle Trajectory and Icing Analysis of the E3 Turbofan Engine Using LEWICE3D Version 3, NASA/TM–2012-217696, NASA.
Demartino, C., Koss, H.H., Ricciardelli, F., 2013. Experimental study of the effect of icing on the aerodynamics of circular cylinders - Part I: cross flow. In: 6th European and African Wind Engineering Conference.
Elkhoury, M., 2016. Assessment of turbulence models for the simulation of turbulent flows past bluff bodies. J. Wind Eng. Ind. Aerod. 154, 10–20.
Finstad, K.J., Lozowski, E.P., Gates, E.M., 1988. A computational investigation of water droplet trajectories. J. Atmos. Ocean. Technol. 5, 160–170. https://doi.org/10.1175/1520-0426(1988)005<0160:ACIOWD>2.0.CO;2.
CE User Manual.
Fluent User Manual.
Fu, P., Farzaneh, M., Bouchard, G., 2006. Two-dimensional modelling of the ice accretion process on transmission line wires and conductors. CRST 46, 132–146.
Gerrard, J.H., 1961. An experimental investigation of the oscillating lift and drag of a circular cylinder shedding turbulent vortices. J. Fluid Mech. 11 (2), 244–256.
Gopalkrishnan, R., 1992. Vortex-Induced Forces on Oscillating Bluff Cylinders. Ph.D. Thesis. MIT/WHOI. WHOI-92-38.
ISO 12494:2001(E), 2001. Atmospheric Icing of Structures. Standard. International Organization for Standardization, Geneva, CH.
Jones, K.F., 1990. The density of natural ice accretions related to nondimensional icing parameters. Q. J. R. Meteorol. Soc. 116, 477–496.
Keyhan, H., 2012. Fluid Structure Interaction (FSI) Based Wind Load Modeling for Dynamic Analysis of Overhead Transmission Lines. Ph.D. Thesis. Department of Civil Engineering and Applied Mechanics, McGill University.
Makkonen, L., 1984. Modeling of ice accretion on wires. J. Appl. Meteorol. 23, 929–939. https://doi.org/10.1175/1520-0450(1984)023<0929:MOIAOW>2.0.CO;2.
Makkonen J., L., Stallabrass R., J., 1984. Ice Accretion on Clyinders and Wires. National Research Council Canada, Canada, pp. 1–50. Technical Report TR-LT-005.
Makkonen, L., Stallabrass, J.R., 1987. Experiments on the cloud droplet collision efficiency of cylinders. J. Appl. Meteorol. 26, 1406–1411. https://doi.org/10.1175/1520-0450(1987)026<1406:EOTCDC>2.0.CO;2.
Menter, F.R., 1994. Two-equation Eddy-viscosity turbulence models for engineering applications. AIAA J. 32 (8), 1598–1605. https://doi.org/10.2514/3.12149. Bibcode: 1994AIAAJ..32.1598M.
Norberg, C., 2002. Fluctuating lift on a circular cylinder: review and new measurements. J. Fluid Struct. 17, 57–96.
Papadakis, M., Wong, S.-C., Rachman, A., October 2007. Large and Small Droplet Impingement Data on Airfoils and Two Simulated Ice Shapes, NASA/TM—2007-213959.
Rossi, A., Jubayer, C., Koss, H., Arriaga, D., Hangan, H., 2020. Combined effects of wind and atmospheric icing on overhead transmission lines. J. Wind Eng. Ind. Aerod. 204.
Selvam, R.P., 1997. Finite element modelling of flow around a circular cylinder using LES. J. Wind Eng. Ind. Aerod. 67&68, 129–139.
Shin, J., Bond, T., 1992. Experimental and computational ice shapes and resulting drag increase for a NACA 0012 airfoil. NASA Technical Manual 105743, 1992.
Tanida, Y., Okajima, A., Watanabe, Y., 1973. Stability of a circular cylinder oscillating in uniform flow or in a wake. J. Fluid Mech. 61 (4), 769–784.
Tritton, D.J., 1988. Physical Fluid Dynamics, second ed. Oxford University Press, Oxford, England.
Wright, W., 2008. User's Manual for LEWICE Version 3.2, NASA/CR–2008-214255, NASA.